Available online at www.sciencedirect.com
ScienceDirect
Trans. Nonferrous Met. Soc. China 35(2025) 3985−4006
Transactions of Nonferrous Metals Society of China
www.tnmsc.cn

A new test method for friction in incremental sheet forming

Guang-can YANG, Da-wei ZHANG, Chong TIAN, Sheng-dun ZHAO

School of Mechanical Engineering, Xi'an Jiaotong University, Xi'an 710049, China

Received 5 March 2024; accepted 1 July 2024

Abstract: An analytical model for contact area and contact stress considering the loading history in incremental sheet forming (ISF) was established. Then, by integrating with the directional characteristics of friction force and horizontal force in the process, a friction test method reflecting the forming characteristics of ISF was proposed. Friction coefficients during the forming processes of parts with different wall angles were measured under various plane curves, process paths, and lubrication conditions. Furthermore, the accuracy of the analytical model, as well as the measured friction coefficients and their variation trends, was verified through comparative analysis with experimental results, simulation data, and outcomes from other existing models. The results indicate that the influence of the plane curve characteristics and process paths of parts on the friction condition is not significant. Under the lubrication conditions of L-HM46 oil, MoS_2 grease, graphite powder, and dry friction, the friction coefficient shows a gradually increasing trend. Notably, when the wall angle is ≤40°, the friction coefficient remains relatively constant; however, when the wall angle exceeds 40°, the friction coefficient increases progressively.

Key words: incremental sheet forming; friction test method; contact area; friction coefficient; forming force

1 Introduction

Since the concept of incremental sheet forming (ISF) was proposed [1−3], the understanding of friction characteristics has remained limited despite remarkable progress in formability [4], accuracy [5] and surface quality [6] research. The point-by-point processing in ISF involves high-pressure contact areas, inducing substantial friction during relative motion [7]. This friction can affect formability and surface quality [8,9]. Thus, a comprehensive study on friction is crucial to enhancing surface quality and supporting the industrial adoption of ISF.

In ISF, process parameters and lubrication conditions critically influence interface friction, affecting part surface quality and formability. Light interferometry scans revealed that the step depth remarkably increases peak-to-valley height, while spindle speed has minimal effect on roughness [10]. Although progress has been made, the friction mechanism in ISF is still not fully understood. DURANTE et al [11] developed a theoretical method for predicting surface roughness, incorporating tool radius, depth increment, and forming angle, but neglected sheet thickness, material properties, and contact conditions. Lubrication improves friction and surface quality [12], but is challenged by lubricant expulsion under high pressure. HUSSAIN et al [13] examined tool−lubricant interactions, emphasizing the need for a detailed mechanism explanation. KIM and PARK [14] found that a spherical tool enhances the formability in AA1050 material without lubrication, though poor interfacial friction leads to early sheet failure. AZEVEDO et al [15] demonstrated that optimal lubricant selection improves surface quality and geometric accuracy and reduces forming force in AA1050 and DP780 steel sheets. Additionally, the role of friction in altering surface characteristics has been recognized

Corresponding author: Da-wei ZHANG, Tel: +86-29-82668607; Fax: +86-29-82665204; E-mail: zhangdawei2000@mail.xjtu.edu.cn
https://doi.org/10.1016/S1003-6326(25)66925-1

in other forming processes [16], highlighting its importance in plastic forming [17,18].

Friction leads to through-thickness shear and twisting of parts in ISF. BAMBACH [19] noted that thickness-shear depends on tool diameter and step size, which accumulates and twists the part, adversely affecting its geometric accuracy. ALLWOOD et al [20] found that through-thickness shear along the tool's movement direction improves the forming limit. EYCKENS et al [21] suggested that tool rotation affects through-thickness shear. CHANG and CHEN [22] developed a new model for the twisting angle in ISF, identifying that uneven circumferential friction stress along the meridional direction causes twisting, with its direction dependent on the derivative of through-thickness stress relative to the wall angle. CARRINO et al [23] etched two orthogonal lines on the sheet, showing that tangential friction twists the part around its axis. This twisting angle at the part's bottom serves as a quantitative friction force indicator. JACKSON and ALLWOOD [24] used a roller tool to convert sliding friction at the tool−sheet interface into rolling friction, thereby reducing thickness shear from friction.

The friction effect plays a crucial role in the forming process, necessitating accurate measurement of friction conditions to study its effect effectively. Various friction test methods have been developed for sheet metal forming. For instance, a tension-bending friction test method [25] employs a tensile strip of sheet metal pulled through a round roll at a specified speed, which is commonly used to evaluate the friction between the sheet metal and the die fillet in stamping [26]. ANDREASEN et al [27] introduced a strip reduction testing method to replicate friction conditions between the sheet metal and the cone mold during forming. NINE [28] designed a device to simulate the drawbead, conducting friction tests on it [29]. Additionally, WANG and WAGONER [30] created an experimental approach to mimic the friction at the punch fillet in sheet metal bulging, considering lubrication effects. This method can simulate actual deformation and contact conditions. However, given that ISF features localized forming characteristics distinct from traditional sheet metal forming, these existing friction test methods are not suitable for ISF.

HAMILTON [31] proposed that the friction force results from normal indentation, tangential sliding, and tool rotation. SILVA et al [32] offered a contact stress analysis model considering plane friction effects under the assumption of plane strain and biaxial equal tension. The model decomposed friction stress into circumferential and radial directions, with circumferential stress generated by the combined action of the circumferential feed and tool rotation, and radial stress primarily influenced by the vertical movement of the tool. However, further research is needed for predicting forming and friction forces. LU et al [33] established a stress model using the membrane analysis method, considering the effect of circumferential friction on the stress state, forming load, and stress triaxiality in ISF. This model provides a foundation for the force prediction. Current methods for characterizing friction conditions in ISF primarily use the horizontal-to-vertical force ratio, as adopted by LU et al [33] and LI et al [34], as a friction indicator to assess tribological behavior under different contact conditions. DURANTE et al [35] found that the friction condition could be characterized by the friction indicator in the straight groove test. The indicator was also used in laser-assisted ISF by XU et al [36] to evaluate the influence of friction on the formability at tool rotation speeds below 1000 r/min. However, the horizontal force measured in these friction experiments includes friction and plastic deformation forces. Consequently, the horizontal force does not represent the true friction force and cannot quantitatively evaluate friction conditions.

The contact area dynamically changes due to the inflow of undeformed materials and outflow of deformed materials in ISF. This results in distinct friction characteristics compared with other processes. However, existing friction test methods fail to capture these specific characteristics. In response, this study introduces a semi-analytical friction test method according to horizontal force balance. By integrating models for contact area, contact stress, and friction directions specific to ISF, this method offers a more accurate reflection of ISF characteristics. The investigation delves into the influence of various wall angles, plane curves, process paths, and lubrication conditions on friction test results. This method is expected to provide a theoretical reference for the evaluation of friction conditions in ISF and a solution to performing test.

2 Semi-analytical friction test method for ISF

This section introduces a new semi-analytical friction test method for ISF, as depicted in Fig. 1. Firstly, an analytical model of the instantaneous contact area that accounts for deformation history, is established. Next, a model for contact stress is developed. These models are then combined to create an analytical model of deformation and friction forces, integrating the directional characteristics of forces in ISF. This integration forms a comprehensive model of the forming force, including deformation and friction forces. Finally, the friction coefficient is calculated by correlating the actual forming force from experimental tests with the analytical model.

2.1 Analytical model of contact area

Accurately evaluating the contact area's size and shape is crucial to calculating the friction and forming forces in ISF. Some researchers approximated the contact area as a rectangle in a CAD model [37]. BANSAL et al [38] modified this model by confirming the geometric relationship between the tool and sheet. CHANG et al [39] introduced models for circumferential, axial, and radial contact areas and deformation forces. Recently, an improved model has been developed for calculating contact areas based on real contact parameters [40]. However, the influence of adjacent forming layers on the contact area remains unaddressed, indicating that the theory of calculating contact area in ISF still requires refinement.

The contact area, detailed in Fig. 2, is influenced by several factors: tool radius (R), initial sheet thickness (t_0), wall angle (α), and depth increment (Z). The size of the contact zone is especially magnified to highlight the geometric features. The contact area S includes S_e and S_h. S_e is the contact sub-area, consisting of the indentation contact area generated by depth increment and the extrusion contact area between the tool and the surface scallop. S_h is the extrusion contact area

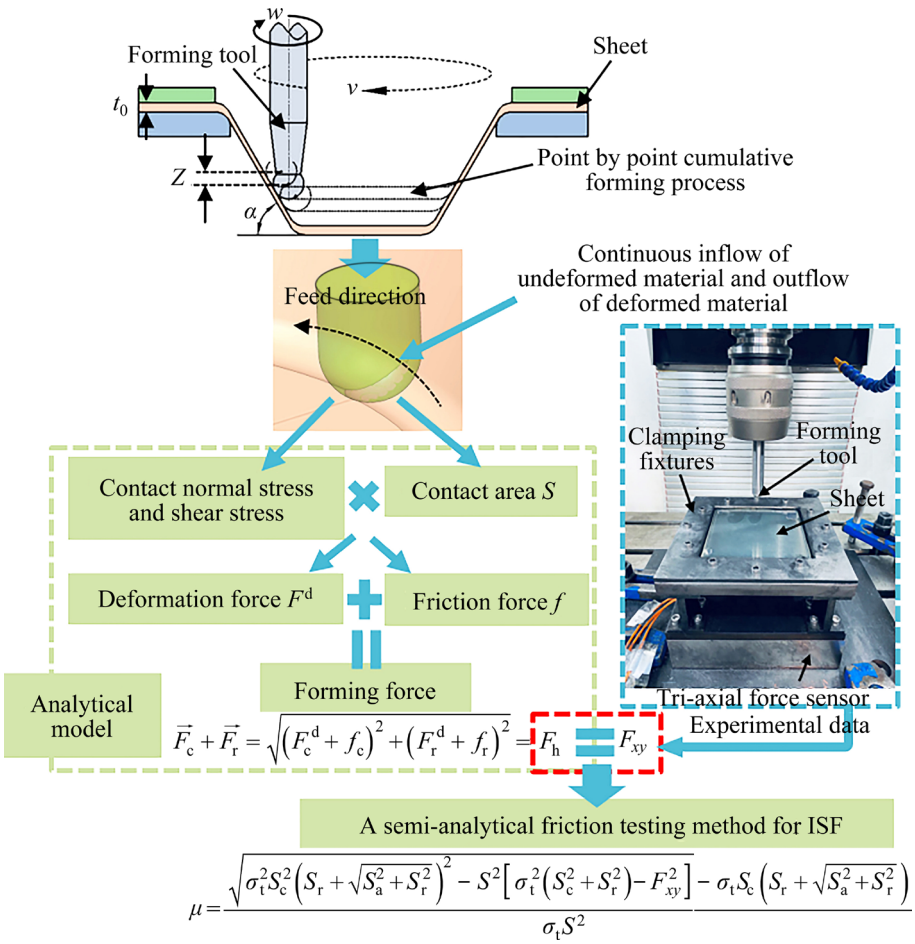

Fig. 1 Procedure of friction test method for ISF

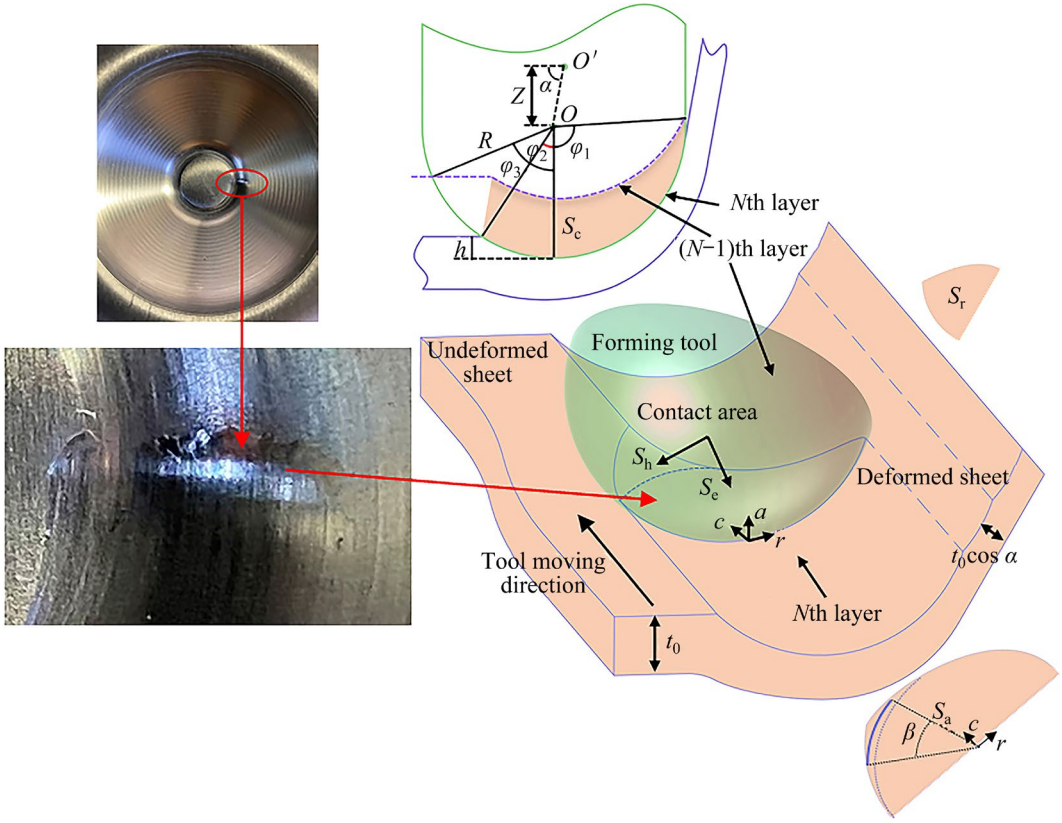

Fig. 2 Schematic diagram of contact area and its projected components of ISF

formed when the undeformed material near the deformation area of the (N−1)th forming layer flows into the deformation area of the Nth forming layer. On the basis of the above analysis and under the assumption that the end of the extruded area of the sheet is tangent to the tool in the meridian direction, a modified contact area model considering the loading history of the previous forming layer is established.

S_e can be calculated by Eq. (1) described in Ref. [39]. The height, denoted as h, represents the extent to which the sheet flows into the bottom of the tool. It can be calculated using Eq. (2) and consists of two distinct components. Firstly, the height increase is attributed to the elastic deflection occurring within the contact area of the sheet metal. Secondly, the height decrease arises from the thinning effect experienced by the sheet. φ_1 and φ_2 are the included angles of the contact area along the meridian direction and can be calculated by Eqs. (3) and (4), respectively:

$$S_e=\frac{\pi}{2}R\left[h+R\frac{(1-\cos\alpha)\varphi_2}{\varphi_1}\right] \tag{1}$$

$$h=\frac{t_0(1-\cos\alpha)}{\alpha\left(3-\frac{\pi}{2}\right)+1}+\sqrt{\frac{2Zt_0}{R}} \tag{2}$$

$$\varphi_1=\alpha+\arcsin\left(\frac{Z}{2R\sin\alpha}\right) \tag{3}$$

$$\varphi_2=\arccos\left(\frac{R-h}{R}\right) \tag{4}$$

When the loading history is considered, S_h can be calculated using Eq. (5) by employing geometric relationships, which can be viewed as the integration of narrow strips along the circumferential direction on the spherical surface of the tool, in the meridional direction.

$$S_h=\int_{\varphi_2}^{\varphi_3}R^2\sin\varphi\cdot\beta\mathrm{d}\varphi \tag{5}$$

where φ is the contact angle along the meridian direction; φ_3 is the wrapping angle along the meridian direction when the material of the (N−1)th forming layer enters the Nth forming layer, which can be calculated by Eq. (6); β is the wrapping angle of S_h along the circumference, which can be calculated by Eq. (7):

$$\varphi_3=\arccos\left(\frac{R-2h}{R}\right) \tag{6}$$

$$\beta=\arccos\left(\frac{\sqrt{R^2-\left(Z+R\cos\varphi\right)^2}-\dfrac{Z}{\tan\alpha}}{R\sin\varphi}\right)-\arccos\left(\frac{\sqrt{R^2-\left(R-h\right)^2}-\dfrac{R-R\cos\varphi-h}{\tan\alpha}}{R\sin\varphi}\right) \tag{7}$$

Based on the above analysis, the contact area S can be calculated by

$$S=S_e+S_h=\frac{\pi}{2}R\left[h+R\frac{(1-\cos\alpha)\varphi_2}{\varphi_1}\right]+\int_{\varphi_2}^{\varphi_3}R^2\sin\varphi\cdot\beta\mathrm{d}\varphi \tag{8}$$

Given that the relative motion between the tool and the sheet is complex, determining the direction of friction is difficult. Therefore, the contact area is projected into axial, circumferential and radial directions (Fig. 2). The complex relative motion is simplified into each projection area to obtain the simple relative motion relationship. The theoretical guidance for the direction of friction action is given. The axial projected area S_a, the circumferential projected area S_c and the radial projected area S_r can be calculated by

$$S_a=\sqrt{R^2-\left(R-h\right)^2}\cdot\left[\frac{\pi}{4}R\sin\varphi_1+\sqrt{R^2-\left(R-h\right)^2}-\frac{Z}{2\tan\alpha}\right] \tag{9}$$

$$S_c=\frac{1}{2}\left[\left(\frac{2+\pi}{2}h+R\right)\sqrt{R^2-\left(R-h\right)^2}+\frac{\pi}{2}hR\sin\varphi_1-R^2\varphi_2+\frac{h^2}{\tan\alpha}\right] \tag{10}$$

$$S_r=\frac{\pi}{4}\sqrt{R^2-\left(R-h\right)^2}\cdot\left(R-R\cos\varphi_1-h\right) \tag{11}$$

2.2 Analytical model of contact stress

As the tool radius is far greater than the sheet thickness, as shown in Fig. 3(a), the stress state is

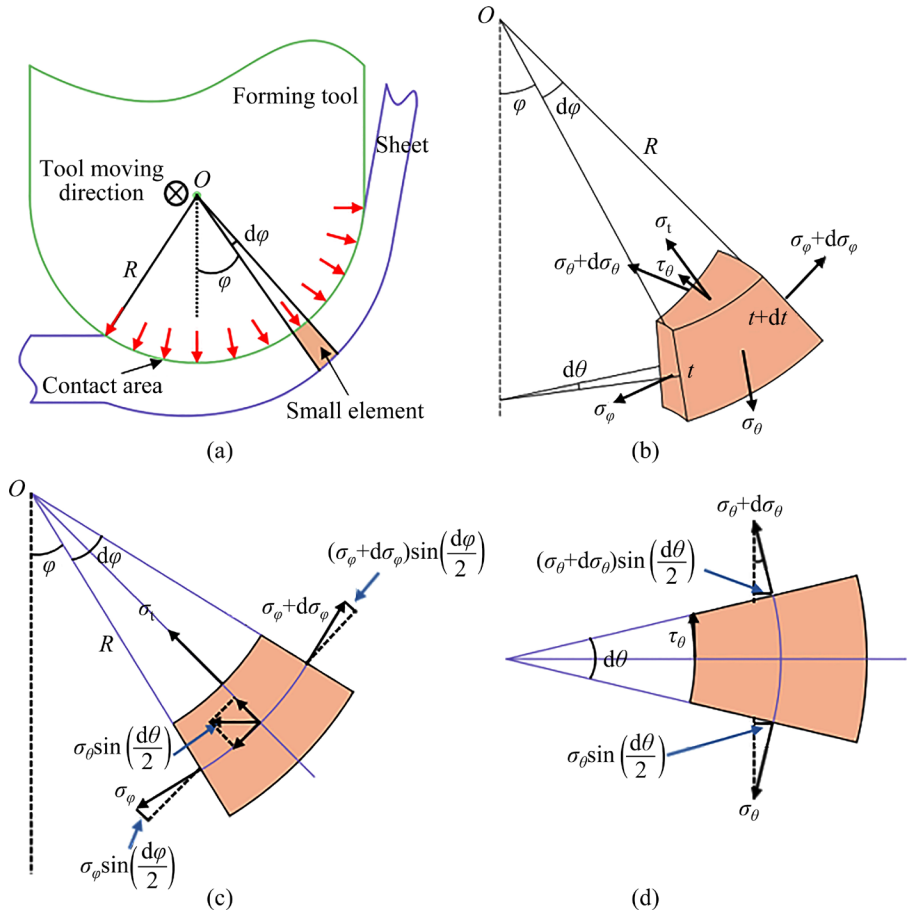

Fig. 3 Diagrams of stress: (a) Overview; (b) Stress components; (c) Meridional direction of (b); (d) Circumferential direction of (b)

analyzed based on the membrane analysis method [32]. The stress components of an element are described in detail in Fig. 3(b): σ_t is the thickness direction stress, σ_φ is the meridian direction stress, σ_θ is the circumferential direction stress, and τ_{θ} is the circumferential shear stress. The influence of the thickness directional shear stress τ_t and the meridional shear stress τ_φ on the deformation area, which is not discussed in this study, can be ignored [33]. The stress states of the element along the meridian and circumferential directions are shown in Figs. 3(c) and (d), respectively. The included angles of the element in the meridian and differential directions are $d\varphi$ and $d\theta$, respectively. Based on the basic assumptions commonly used in plastic processing mechanics and membrane analysis method of ISF, the following reasonable assumptions can be made [32,33,39]:

(1) Compared with the sheet's material properties, the tool can be assumed to be rigid without deformation.

(2) σ_t is evenly distributed along the circumferential and meridian directions on the contact surface. That is, σ_t is independent of the circumferential angle θ and meridian angle φ.

(3) σ_t is linearly distributed along the thickness direction; thus, the outer surface of the sheet is 0.

(4) The shear stress can be expressed as $\tau_\theta=\mu\sigma_t$ and evenly distributed in the contact area, where μ is the friction coefficient during ISF.

The force component acted by σ_t on the neutral plane along the thickness direction in the element is

$$F_{\sigma_t}^{t}=\frac{\sigma_t}{2}\cdot\left(R+\frac{t}{2}+\frac{dt}{4}\right)d\varphi\cdot\left(R+\frac{t}{2}+\frac{dt}{4}\right)\sin\left(\varphi+\frac{d\varphi}{2}\right)d\theta \tag{12}$$

where t is the actual sheet thickness, which can be expressed as

$$t=t_0\cos\alpha \tag{13}$$

The force component along the thickness direction generated by the action of σ_φ on the element is

$$F_{\sigma_\varphi}^{t}=\left(\sigma_\varphi+d\sigma_\varphi\right)\cdot\left(R+\frac{t+dt}{2}\right)\sin\left(\varphi+d\varphi\right)d\theta\cdot\left(t+dt\right)\sin\left(\frac{d\varphi}{2}\right)+\sigma_\varphi\left(R+\frac{t}{2}\right)\sin\varphi\cdot d\theta\cdot t\sin\left(\frac{d\varphi}{2}\right) \tag{14}$$

The force component along the thickness direction generated by the action of σ_θ on the element is

$$F_{\sigma_\theta}^{t}=\left(2\sigma_\theta+d\sigma_\theta\right)\left(R+\frac{t}{2}+\frac{dt}{4}\right)d\varphi\cdot\left(t+\frac{dt}{2}\right)\cdot\sin\left(\frac{d\theta}{2}\right)\cdot\sin\left(\varphi+\frac{d\varphi}{2}\right) \tag{15}$$

The force balance equation along the thickness direction on the neutral plane of the element can be expressed as

$$F_{\sigma_t}^{t}+F_{\sigma_\varphi}^{t}+F_{\sigma_\theta}^{t}=0 \tag{16}$$

Given that $d\varphi$ and $d\theta$ are small, $\sin(d\varphi/2)\approx d\varphi/2$, $\sin(d\theta/2)\approx d\theta/2$, $R \gg t$; with higher-order terms neglected and the plane strain state combined, the simplified form of Eq. (16) is obtained by

$$\sigma_t\left(R+\frac{t}{2}\right)+2t\sigma_\varphi=0 \tag{17}$$

The Tresca yield criterion is

$$\sigma_\varphi-\sigma_t=\sigma_e \tag{18}$$

where σ_e is the equivalent yield stress.

After combining Eqs. (17) and (18), the relationship between σ_t and the equivalent yield stress σ_e is obtained by

$$\sigma_t=-\frac{2t}{R+\frac{5}{2}t}\sigma_e \tag{19}$$

The strain in the meridian direction ε_φ is caused by tension and bending on the neutral plane of the sheet, which can be derived by

$$\varepsilon_\varphi=\ln\left(\frac{t_0}{t}\right)+\ln\left(\frac{R}{R+\frac{t}{2}}\right)=\ln\left(\frac{Rt_0}{t\left(R+\frac{t}{2}\right)}\right) \tag{20}$$

Based on the principle of constant volume and plane strain assumption, the thickness strain ε_t is

$$\varepsilon_t=-\varepsilon_\varphi \tag{21}$$

Therefore, the equivalent plastic strain ε_e in the deformation zone can be calculated by

$$\varepsilon_e=\frac{2}{\sqrt{3}}\ln\left[\frac{Rt_0}{t\left(R+\frac{t}{2}\right)}\right] \tag{22}$$

The equivalent plastic stress σ_e can be expressed in accordance with the constitutive equation of materials:

$$\sigma_e=\text{Func}(\varepsilon_e) \tag{23}$$

The analysis model of equivalent plastic stress σ_e about key forming parameters and material properties can be established by combining Eqs. (22) and (23). Furthermore, by substituting Eq. (23) into Eq. (19), the thickness directional contact stress σ_t is expressed as

$$\sigma_t=-\frac{2t}{R+\frac{5}{2}t}\cdot\text{Func}\left\{\frac{2}{\sqrt{3}}\ln\left[\frac{Rt_0}{t\left(R+\frac{t}{2}\right)}\right]\right\} \tag{24}$$

Therefore, the tangential friction stress (τ) can be calculated by

$$\tau=\mu\sigma_t=\mu\frac{2t}{R+\frac{5}{2}t}\cdot\text{Func}\left\{\frac{2}{\sqrt{3}}\ln\left[\frac{Rt_0}{t\left(R+\frac{t}{2}\right)}\right]\right\} \tag{25}$$

2.3 Deformation force and friction force

In ISF, the material deformation force is the integral of the contact stress on the contact area. Therefore, the axial deformation force F_a^d, the radial deformation force F_r^d, and the circumferential deformation force F_c^d can be obtained by combining the axial projected contact area S_a, the radial projected area S_r, and the circumferential projected area S_c with the thickness contact stress σ_t as follows:

$$F_a^d=\sigma_t S_a=\frac{2t}{R+\frac{5}{2}t}\cdot\text{Func}\left[\frac{2}{\sqrt{3}}\ln\left(\frac{Rt_0}{R+\frac{t}{2}}\right)\right]\cdot\sqrt{R^2-(R-h)^2}\cdot\left[\frac{\pi}{4}R\sin\varphi_1+\sqrt{R^2-(R-h)^2}-\frac{Z}{2\tan\alpha}\right] \tag{26}$$

$$F_r^d=\sigma_t S_r=\frac{2t}{R+\frac{5}{2}t}\cdot\text{Func}\left\{\frac{2}{\sqrt{3}}\ln\left[\frac{Rt_o}{t\left(R+\frac{t}{2}\right)}\right]\right\}\cdot\frac{\pi}{4}\sqrt{R^2-(R-h)^2}\cdot(R-R\cos\varphi_1-h) \tag{27}$$

$$F_c^d=\sigma_t S_c=\frac{2t}{R+\frac{5}{2}t}\cdot\text{Func}\left\{\frac{2}{\sqrt{3}}\ln\left[\frac{Rt_0}{t\left(R+\frac{t}{2}\right)}\right]\right\}\cdot\left\{\frac{1}{2}\left[\left(\frac{2+\pi}{2}h+R\right)\sqrt{R^2-(R-h)^2}+\frac{\pi}{2}hR\sin\varphi_1-R^2\varphi_2+\frac{h^2}{\tan\alpha}\right]\right\} \tag{28}$$

The total deformation force F^d during ISF can be calculated by

$$F^d=\sigma_t S=\frac{2t}{R+\frac{5}{2}t}\cdot\text{Func}\left\{\frac{2}{\sqrt{3}}\ln\left(\frac{Rt_0}{t\left(R+\frac{t}{2}\right)}\right)\right\}\cdot\left\{\frac{\pi}{2}R\left[h+R\frac{(1-\cos\alpha)\varphi_2}{\varphi_1}\right]+\int_{\varphi_2}^{\varphi_3}R^2\sin\varphi\cdot\beta\,\mathrm{d}\varphi\right\} \tag{29}$$

When the friction coefficient is μ, the total friction force f in ISF can be calculated by

$$f=\mu F^d=\mu\frac{2t}{R+\frac{5}{2}t}\cdot\text{Func}\left\{\frac{2}{\sqrt{3}}\ln\left[\frac{Rt_0}{t\left(R+\frac{t}{2}\right)}\right]\right\}\cdot\left\{\frac{\pi}{2}R\left[h+R\frac{(1-\cos\alpha)\varphi_2}{\varphi_1}\right]+\int_{\varphi_2}^{\varphi_3}R^2\sin\varphi\cdot\beta\,\mathrm{d}\varphi\right\} \tag{30}$$

As shown in Fig. 4, the friction force f includes the circumferential friction force f_w introduced by spindle rotation and the meridian directional friction force f_f generated by the feed motion. f_w can be divided into horizontal circumferential component f_w^c and radial component f_w^r, but has no axial component. f_f can be divided into axial component f_f^a and circumferential component f_f^c, where f_f^a acts on S_c, and f_f^c acts on S_a. Given that the depth increment Z is far less than the tool radius R, resulting in S_c being far less than S_a, f_f^c is far greater than f_f^a, thus, f_f^a can be ignored, that is, $f_f^c\approx f_f$. Based on the above analysis, the friction effect in ISF is inferred to be distributed in the horizontal direction. Therefore, the shear deformation of the part along the feed direction is caused by the friction traction

force [33], which even leads to the twisting of the part [41], while along the meridian direction of the tool, the primary deformation is tensile, and the shear deformation is not remarkable.

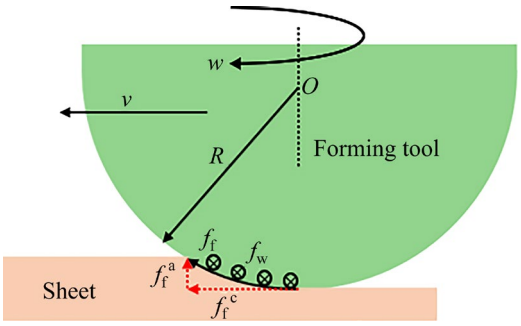

Fig. 4 Schematic diagram of direction of friction force and its components in ISF

Therefore, the circumferential component of friction force f_c acts on the axial projected area S_a and radial projected area S_r, as the vector sum of f_w^c and f_f^c, which can be calculated by

$$f_c=\overrightarrow{f_w^c}+\overrightarrow{f_f^c}=\mu\sigma_t\sqrt{S_a^2+S_r^2} \tag{31}$$

By substituting Eqs. (9), (11), and (24) into Eq. (31), we have

$$f_c=\mu\frac{2t}{R+\frac{5}{2}t}\cdot\mathrm{Func}\left\{\frac{2}{\sqrt{3}}\ln\left[\frac{Rt_0}{t\left(R+\frac{t}{2}\right)}\right]\right\}\sqrt{R^2-(R-h)^2}\cdot$$
$$\left[\left(\frac{\pi}{4}R\sin\varphi_1+\sqrt{R^2-(R-h)^2}-\frac{Z}{2\tan\alpha}\right)^2+\right.$$
$$\left.\frac{\pi^2}{16}\left(R-R\cos\varphi_1-h\right)^2\right]^{1/2} \tag{32}$$

The radial friction force f_r acts on the circumferential projection area S_c, $f_r\approx f_w^r$, which can be calculated by

$$f_r=f_w^r=\tau_\theta S_c=\mu\frac{2t}{R+\frac{5}{2}t}\cdot\mathrm{Func}\left\{\frac{2}{\sqrt{3}}\ln\left[\frac{Rt_0}{t\left(R+\frac{t}{2}\right)}\right]\right\}\cdot$$
$$\frac{1}{2}\left[\left(\frac{2+\pi}{2}h+R\right)\sqrt{R^2-(R-h)^2}+\right.$$
$$\left.\frac{\pi}{2}hR\sin\varphi_1-R^2\varphi_2+\frac{h^2}{\tan\alpha}\right] \tag{33}$$

2.4 Forming force

According to the analysis in Section 2.3, the friction effect in ISF mainly acts in the horizontal direction, and its axial component can be ignored. Therefore, the axial forming force (F_a) is almost equal to the axial deformation force F_a^d, that is

$$F_a=F_a^d \tag{34}$$

In ISF, the horizontal forming force (F_h) is the vector operation of the circumferential forming force F_c and the radial forming force F_r. The circumferential forming force F_c is composed of the circumferential deformation force F_c^d and the circumferential friction force f_c. The radial forming force F_r is composed of the radial deformation force F_r^d and the radial friction force f_r. Thus, the relationship can be given by

$$F_h=\overrightarrow{F_c}+\overrightarrow{F_r}=\sqrt{\left(F_c^d+f_c\right)^2+\left(F_r^d+f_r\right)^2} \tag{35}$$

Therefore, the total forming force can be calculated by

$$F=\overrightarrow{F_a}+\overrightarrow{F_h}=\mathrm{Func}\left(\sigma_e,\ \alpha,\ t,\ R,\ Z,\ \mu\right) \tag{36}$$

The loads in the horizontal plane (F_x and F_y) during ISF can be measured by the sensor of the friction test equipment of ISF, as shown in Fig. 5. Thus, the horizontal load (F_{xy}) can be calculated by

$$F_{xy}=\sqrt{F_x^2+F_y^2} \tag{37}$$

where F_x and F_y are the projected components of the circumferential forming force F_c and radial forming force F_r in the x and y axis, respectively; thus, F_{xy} is equal to the horizontal forming force F_h, which can be written by

$$F_h=F_{xy} \tag{38}$$

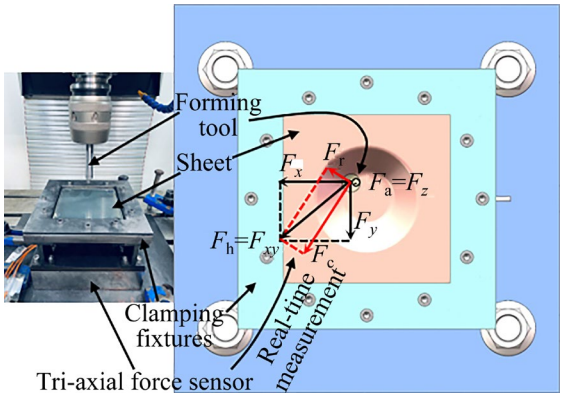

Fig. 5 Sketch of relationship between F_h and F_{xy}

In addition, the load in z-axis (F_z) measured by experiments is equal to the axial forming force F_a, which can be expressed as

$$F_a=F_z \tag{39}$$

2.5 Determination of friction coefficient

According to the equation relationship between the analytical model of horizontal force F_h and the measured value F_{xy} established by Eq. (38), the friction coefficient μ about key forming parameters, material properties and measured horizontal force can be expressed as Eq. (40), by which Eqs. (30)−(33) can be used to calculate the total friction force f, circumferential friction component f_c, and radial friction component f_r.

$$\mu=\left\{\left[\sigma_t^2S_c^2\left(S_r+\sqrt{S_a^2+S_r^2}\right)^2-S^2(\sigma_t^2(S_c^2+S_r^2)-F_{xy}^2)\right]^{1/2}-\sigma_tS_c\left(S_r+\sqrt{S_a^2+S_r^2}\right)\right\}\Big/(\sigma_tS^2) \tag{40}$$

3 Finite element analysis of ISF

The simulation model was established by the dynamic explicit analysis module of ABAQUS, as shown in Fig. 6. The sheet metal dimensions were 200 mm × 200 mm × 1 mm (length × width × thickness), and a local refinement mesh size of 0.5 mm was applied in the potentially processed region. Notably, employing shell elements for the sheet and considering its substantial length and width compared with thickness, computational efficiency was ensured while maintaining accuracy. The material properties of the AA5052-O sheet were derived from material experiments conducted on an Instron−100 kN machine at a quasi-static tensile speed of 0.1 mm/min. These experiments were performed in three directions: parallel to the rolling direction, perpendicular to the rolling direction, and at a 45° angle to the rolling direction of the AA5052-O sheet. Anisotropic effects were deemed negligible, and averaged values from the three directions were used as the mechanical property data, from which the following constitutive equation was determined through fitting:

$$\sigma_e=253.41485-88.85789\exp\left(-\frac{\varepsilon_e}{0.00272}\right)-153.73168\exp\left(-\frac{\varepsilon_e}{0.09745}\right) \tag{41}$$

The tool, with a radius of 7 mm, was considered rigid due to its remarkably higher hardness compared with the sheet, ensuring no plastic deformation during forming. The blank holder and backing plate (Fig. 6), acted as rigid bodies solely for fixing the sheet's position. The backing plate was entirely fixed, while a face load of 5 MN was applied to the blank holder. The friction coefficient between the blank holder/backing plate and the sheet was set to be 0.35. Parameters of the tool feed speed (1000 mm/min), spindle speed (500 r/min) and depth increment (0.5 mm) were chosen in accordance with common practices in practical incremental forming processes. The friction coefficient, determined by the proposed friction testing method in this study, was incorporated into the contact pairs between the sheet and the tool. The penalty function method was employed as the contact algorithm for surface-to-surface contact.

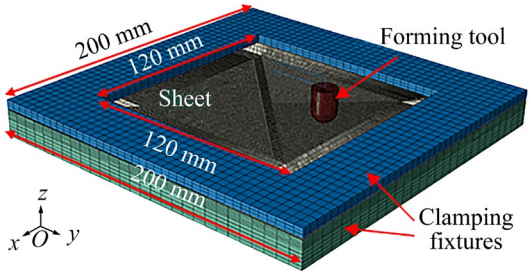

Fig. 6 Schematic diagram of finite element analysis model

4 Friction test experiments for ISF

The schematic diagram of the friction test equipment of ISF is shown in Fig. 7. A sheet is fixed by the blank holder and the backing plate, and an expansion space required for forming parts is provided by the supporting block, which is fixedly connected with the sensor through the connecting plate. The above clamping fixtures are installed on the machine tool slide through the foundation. A tool can be driven by the machine tool spindle to move according to the pre-designed path. During ISF, the loads along the x, y, and z axes are detected by the strain elements of the sensor, which cause

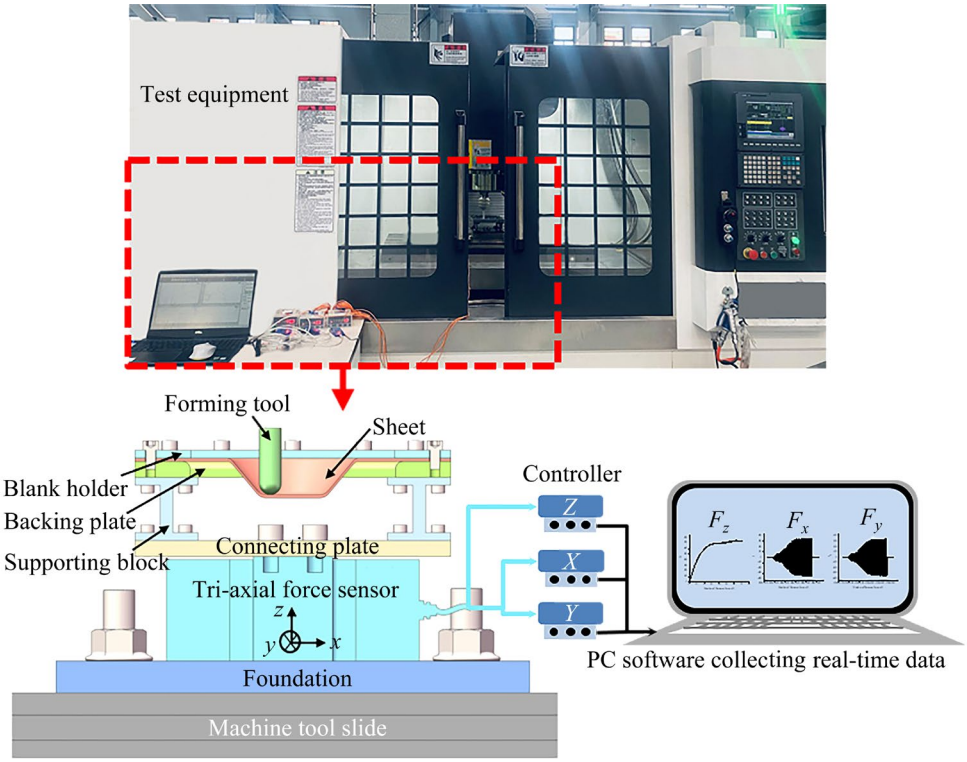

Fig. 7 Schematic diagram of friction test equipment

electrical signals to change in real-time. The electrical signals are converted into digital signals by the controllers transmitted to the upper computer software to display the loads F_x, F_y, and F_z along x, y, and z-axes in real-time, respectively. The friction coefficient μ under the corresponding experimental conditions can be calculated using Eq. (40).

The friction tests of ISF were conducted under the experimental conditions shown in Table 1. The plane curve and wall angle are the key geometric features of parts. The wall angles of conventional parts are 30°−60°, as shown in Fig. 8(a). Therefore, the friction conditions of conventional wall angles were measured. The plane curves of parts are basically composed of the combinations of circular arcs, straight lines, and variable curvature arcs, while typical truncated cone, truncated pyramid, and truncated elliptic cone (Figs. 8(b−d)) are formed by the accumulation of the above single plane curve along different wall angles. Thus, in this work, the friction conditions of truncated cones, truncated pyramids and truncated elliptic cones were measured, which are suitable for evaluating the friction conditions of parts with various plane curve features. The maximum diameter of the truncated cone D=70 mm, the maximum side length of the truncated pyramid L=100 mm, the maximum major axis L_1=100 mm and the maximum minor axis L_2=70 mm of the truncated elliptic cone were chosen.

Table 1 Fraction experimental parameters and conditions of ISF

Parameter and condition	Value
Forming tool radius, R/mm	7
Initial sheet thickness, t_0/mm	1
Depth increment, Z/mm	0.5
Wall angle, α/(°)	30, 40, 50, 60
Feed speed, v/(mm·min^{-1})	1000
Spindle speed, ω/(r·min^{-1})	500
Plane curve	Circular arc, straight line, and variable curvature arc
Process path	Contour path, and spiral path
Lubricant	L-HM46 oil, MoS_2 grease, graphite particle powder, and dry friction

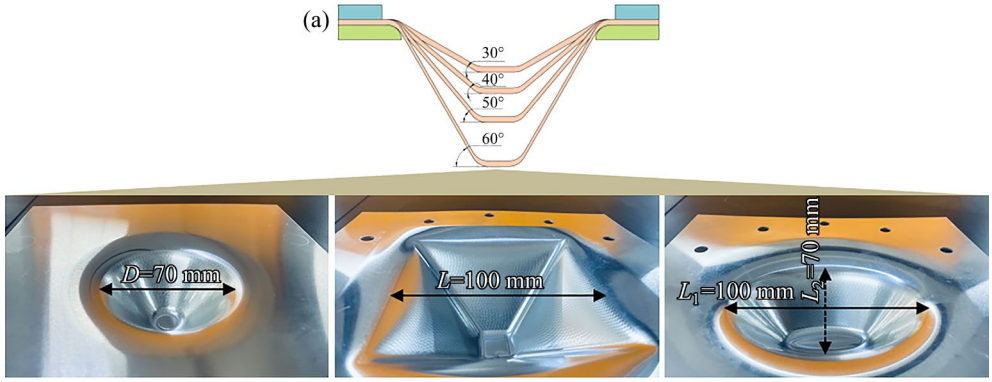

Fig. 8 Geometric features of parts: (a) Wall angle; (b) Truncated cone; (c) Truncated pyramid; (d) Truncated elliptic cone

In addition, the friction conditions of the contour and spiral paths shown in Figs. 9(a) and (b) were tested. Lubrication is one of the most effective methods to improve interface friction conditions. Moreover, anti-wear mechanical lubricating oil L-HM46, MoS_2 grease, graphite nanoparticle powder and dry friction without lubrication are common lubrication conditions for sheet metal forming under various working conditions. The friction conditions under the above lubrication conditions were tested.

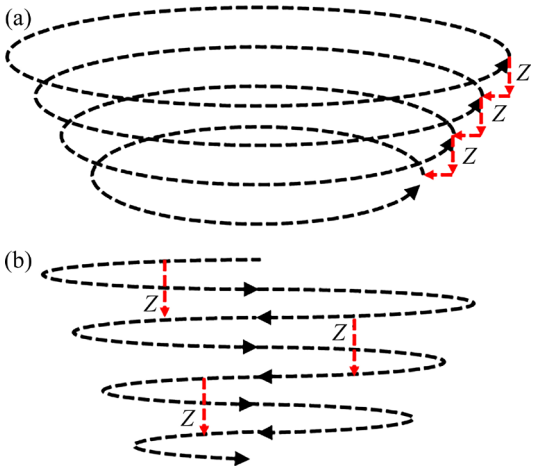

Fig. 9 Schematic diagrams of contour path (a) and spiral path (b)

The friction coefficients for forming truncated cones, truncated pyramids and truncated elliptic cones with different wall angles under the spiral path and L-HM46 oil lubrication conditions are shown in Fig. 10(a). The friction coefficients when forming truncated cone parts with different wall angles under L-HM46 oil lubrication using spiral and contour process paths are shown in Fig. 10(b). In addition, the friction coefficients when forming truncated cone parts with different wall angles by a spiral path under different lubrication conditions are shown in Fig. 10(c). The friction conditions of graphite solid particle powder and dry friction are poor, resulting in the reduced formability of the sheet metal and the inability to form parts with large wall angles, thus, those were not discussed in this work.

5 Results and discussion

5.1 Validation of analytical model

The measured axial forces of parts with different wall angles formed along different plane curves using the spiral process path are depicted in the scatter diagram in Fig. 11(a). The forces for the truncated pyramid and truncated elliptic cone align well with those of the truncated cone, with maximum deviations of 0.437% at α=30°, 0.088% at α=40°, 0.941% at α=50°, and 0.716% at α=60°. The deformation force in ISF is almost unaffected by the type of plane curve.

Comparing measured axial forces with analytical models from Refs. [37−39,42] reveals that the models overestimate the forces. By contrast, the new analytical model demonstrates consistency with the measured values when forming truncated cones, truncated pyramids, and truncated elliptic cones, as shown in Fig. 11(a). The maximum deviation decreases from 33.297% to 4.712% at α=30°, from 42.893% to 1.407% at α=40°, from 48.893% to 1.528% at α=50°, and from 48.195% to 2.707% at α=60°. Thus, the new model exhibits

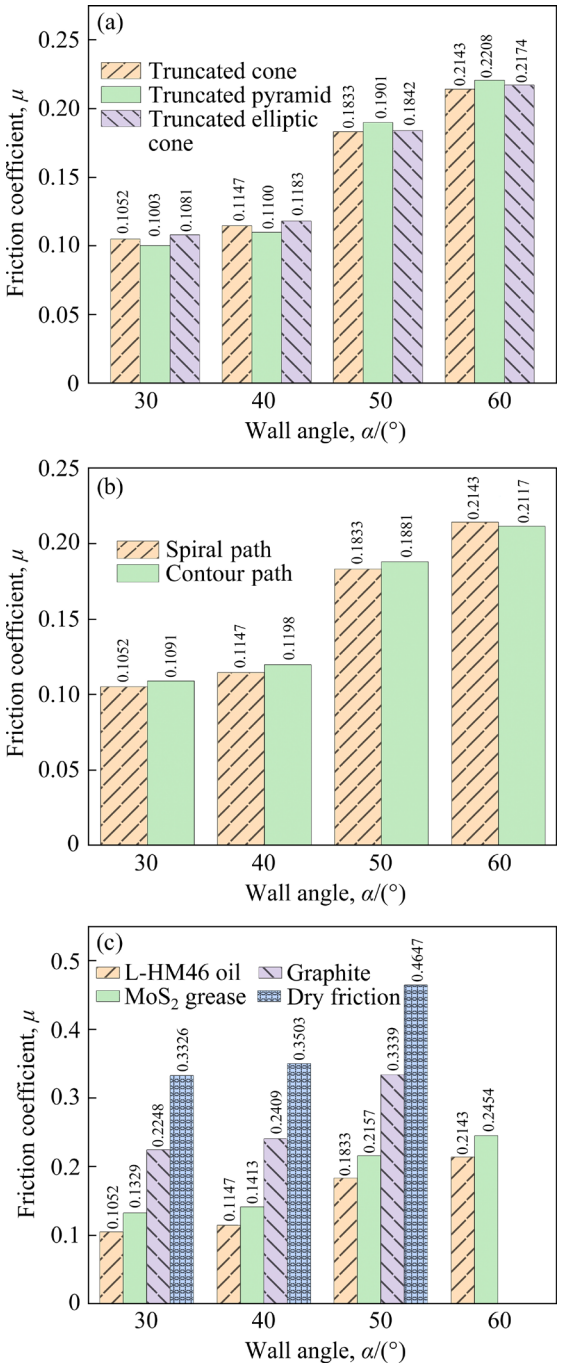

Fig. 10 Friction coefficients under different forming conditions: (a) Different plane curve features; (b) Different process paths; (c) Different lubrication conditions

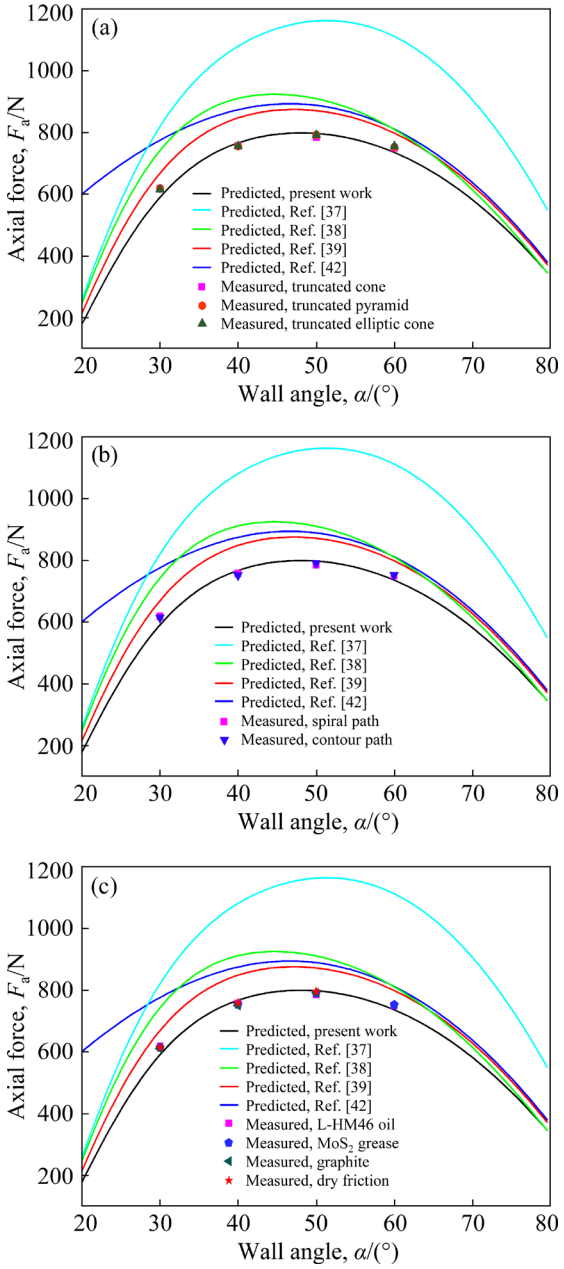

Fig. 11 Axial forces under various forming conditions: (a) Different plane curve features; (b) Different process paths; (c) Different lubrication conditions

the increased accuracy for calculating deformation forces for parts with different wall angles along distinct plane curves.

The measured axial forces when forming truncated cone parts with different wall angles by different process paths are shown in the scatter diagram in Fig. 11(b). The deviation between the spiral path and the contour path is minimal, ranging from 0.736% to 0.247% across wall angles from 30° to 60°. Consequently, the type of process path has negligible influence on the deformation force in ISF.

Similarly, the measured values for the contour process path are substantially smaller than calculated values from existing analytical models [37−39,42]. However, they closely align with the new analytical model, as depicted in Fig. 11(b). The maximum deviation decreases from 33.668% to 3.910% at α=30°, from 43.826% to 2.090% at α=40°, from 48.195% to 0.860% at α=50°, and

from 48.195% to 2.180% at α=60°. This decrease emphasizes the increased calculation accuracy of the new model for deformation forces associated with different process paths.

The axial forces under different lubrication conditions are shown in the scatter diagram in Fig. 11(c). When wall angles are consistent, the experimental data under various lubrication conditions exhibit good agreement, with a maximum deviation of 1.387% at α=30°, 0.988% at α=40°, 1.318% at α=50°, and 0.177% at α=60°. Thus, lubrication conditions show minimal influence on deformation forces in ISF.

Comparing calculated axial forces from analytical models [37−39,42] with the measured values reveals substantial overestimation by the former and poor consistency. However, the new analytical model's calculated values align well with the measured axial forces under different lubrication conditions, as illustrated in Fig. 11(c). The maximum deviation decreases from 34.581% to 4.449% at α=30°, from 44.192% to 2.349% at α=40°, from 48.034% to 1.552% at α=50°, and from 48.195% to 1.938% at α=60°. Consequently, the new analytical model demonstrates the increased calculation accuracy for deformation forces in ISF under diverse lubrication conditions.

5.2 Evaluation of friction test method

According to Eq. (40), the determination of horizontal forming force is a crucial factor in assessing the accuracy of friction coefficients. Therefore, analyzing the evaluation accuracy of horizontal force becomes essential evidence to validate the applicability of the testing method proposed in this study for ISF.

The forming forces of truncated cone, truncated pyramid and truncated elliptic cone, shaped by circular arc, straight line and variable curvature arc, respectively, are shown in the scatter plot in Fig. 12(a). These forces exhibit an initial increase and subsequent decrease with the growing wall angle. However, at identical wall angles, the measured values for different plane curve paths show strong agreement, with minimal deviations of 0.402% at α=30°, 0.274% at α=40°, 0.981% at α=50°, and 0.675% at α=60°. Remarkably, the type of plane curve has minimal influence on the forming force.

For various plane curve features, the forming forces calculated by the new method, excluding friction effects, and other analytical models in Refs. [37−39] are considerably different from experimental measurements, as shown in the line plot in Fig. 12(a). The maximum deviation is 18.121% at α=30°, 10.880% at α=40°, 13.276% at α=50°, and 15.349% at α=60°. Given the omission of friction effects, the calculated values from existing models, except for the one in Ref. [37], are notably smaller than the measured values. Conversely, the model in Ref. [37] overestimates the forming force. Therefore, calculation accuracy must be improved.

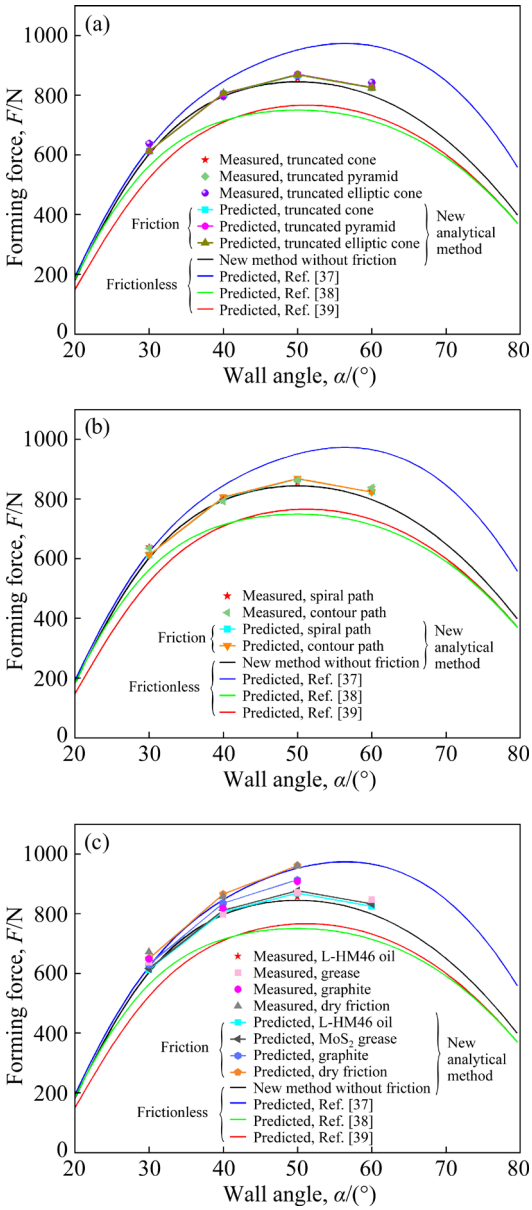

Fig. 12 Forming forces under various forming conditions: (a) Different plane curve features; (b) Different process paths; (c) Different lubrication conditions

Considering friction effects, the predicted values of the new method align well with the measured ones, as shown in the line + symbol plot in Fig. 12(a). The maximum deviation decreases to 4.206% at α=30°, 1.292% at α=40°, 1.304% at α=50°, and 2.110% at α=60°, signifying enhanced prediction accuracy after accounting for friction effects.

The forming forces of truncated cone with different wall angles formed by spiral and contour process paths are presented in the scatter plot in Fig. 12(b). Minimal deviation is observed, ranging from 0.640% at α=30° to 0.116% at α=60°, suggesting that the type of process path has minimal effect on the forming force.

For different process paths, the new method demonstrates high prediction accuracy for spiral and contour paths, as shown in Figs. 12(a) and (b). The forming forces along the contour path, calculated by the new method without considering friction effects and other analytical models from Refs. [37−39], exhibit clear deviations from experimental measurements. However, the new method, when considering friction effects, shows remarkably improved accuracy, with deviations reduced to 3.502% at α=30°, 1.879% at α=40°, 0.723% at α=50°, and 1.749% at α=60°. This result highlights the new method's superior accuracy for predicting forming forces along different process paths after accounting for friction effects.

The scatter plot (Fig. 12(c)) shows the influence of lubrication conditions on forming forces, where forming force is minimal with L-HM46 oil lubrication and increases progressively with MoS_2 grease, graphite powder lubrication, and peaks with dry friction, indicating a direct correlation between higher friction coefficients and increased forming forces. In addition, the smaller the friction coefficient is, the closer the forming force is to the predicted value of the new method without considering the friction effect. Moreover, the predicted values from Refs. [37−39] deviate from the measured values: at α values of 30°, 40°, 50°, and 60°, the maximum deviations with L-HM46 oil lubrication are 18.121%, 10.740%, 12.425%, and 15.349%, respectively; the maximum deviations with MoS_2 grease lubrication are 17.928%, 10.968%, 13.773%, and 15.674%, respectively. At α values of 30°, 40°, and 50°, the maximum deviations with graphite powder lubrication are 19.215%, 13.232%, and 17.262%, respectively; the maximum deviations under dry friction condition are 22.049%, 17.104%, and 21.806%, respectively.

The predicted values reported in Ref. [37] are overestimated, exhibiting significant discrepancies from the measured values under low-friction conditions (L-HM46 oil, MoS_2 grease, and graphite powder lubrication) while aligning closely with the measured values under dry friction. This is paradoxical: since the model neglects frictional effects, its predictions should theoretically be substantially lower than those under dry friction (where frictional effects are most pronounced, leading to the highest measured forming forces). In addition, the predicted values from Refs. [38,39] are too small and do not consider the friction effect. Therefore, the forming forces under varied lubrication conditions cannot be predicted by the above analytical models.

After considering the friction effect, the evaluated forming forces by this study agree well with the measured ones: the deviations at α values of 30°, 40°, 50°, and 60° with L-HM46 oil lubrication are 4.198%, 1.210%, 1.304%, and 1.551%, respectively; the deviations at α values of 30°, 40°, 50°, and 60° with MoS_2 grease lubrication are 3.395%, 1.725%, 0.755%, and 1.657%, respectively; the deviations at α values of 30°, 40°, and 50° with graphite powder lubrication are 2.739%, 1.970%, and 0.705%; the deviations of α values of 30°, 40°, and 50° under dry friction condition are 3.166%, 1.005%, and 0.158%, respectively. Thus, the actual forming forces under different lubrication conditions can be better predicted by the new method after considering the friction effect.

Furthermore, evaluating the friction conditions' accuracy is crucial to precise finite element analysis (FEA). Horizontal forming forces, which vary with friction conditions during ISF, serve as essential criteria for determining friction coefficients. Simulation models incorporating measured friction coefficients demonstrate good agreement with experimental data, confirming the high accuracy of the measured friction conditions.

The simulation data (under the measured friction coefficients as shown in Fig. 10 and the measured friction coefficients increasing or decreasing by 10%) F_h^{FEA} and the measured value

F_h of the horizontal forming forces of the truncated cone with different wall angles are shown in Fig. 13. The forming process gradually reaches a stable state with increasing forming layers. The average value of the data in the stable stage is taken as the horizontal forming force under the corresponding forming condition.

The deviations between F_h^{FEA} under μ=0.1157 (1.1 times of measured value), 0.1052 (measured value) and 0.0947 (0.9 times of measured value), and F_h are 8.446%, 3.301%, and 4.584%, respectively, at α=30°, with the minimum deviation observed at μ=0.1052, as shown in Fig. 13(a). Deviations between F_h^{FEA} under μ=0.126 (1.1 times of measured value), 0.1147 (measured value) and 0.103 (0.9 times of measured value), and F_h are 8.238%, 3.137%, and 4.288%, respectively, at α=40°, with the minimum deviation at μ=0.1147, as shown in Fig. 13(b). Deviations between F_h^{FEA} under μ=0.2016 (1.1 times of measured value), 0.1833 (measured value), and 0.1650 (0.9 times of measured value), and F_h are 5.753%, 1.697%, and 2.505%, respectively, at α=50°, with the minimum deviation at μ=0.1833, as shown in Fig. 13(c). Deviations between F_h^{FEA} under μ=0.2357 (1.1 times of measured value), 0.2143 (measured value) and 0.1929 (0.9 times of measured value), and F_h are 9.746%, 4.502%, and 5.245%, respectively, at α=60°, with the minimum deviation at μ=0.2143, as shown in Fig. 13(d). The simulation results agree well with the measured values when friction coefficients match the experimentally determined values. Additionally, deviations increase when friction coefficients increase or decrease by 10%. This result confirms the high accuracy of the measured friction conditions.

5.3 Influence of forming parameters on friction conditions

LU et al [33] and XU et al [36] evaluated the friction condition in ISF with friction indicator μ^*, which is the ratio of the measured horizontal force (F_h) to vertical force F_z, as shown in Eq. (42). However, friction force and deformation force are included in the measured horizontal force. Although this friction indicator does not directly represent the true friction condition, its variation trend can be utilized to verify the reliability of the friction

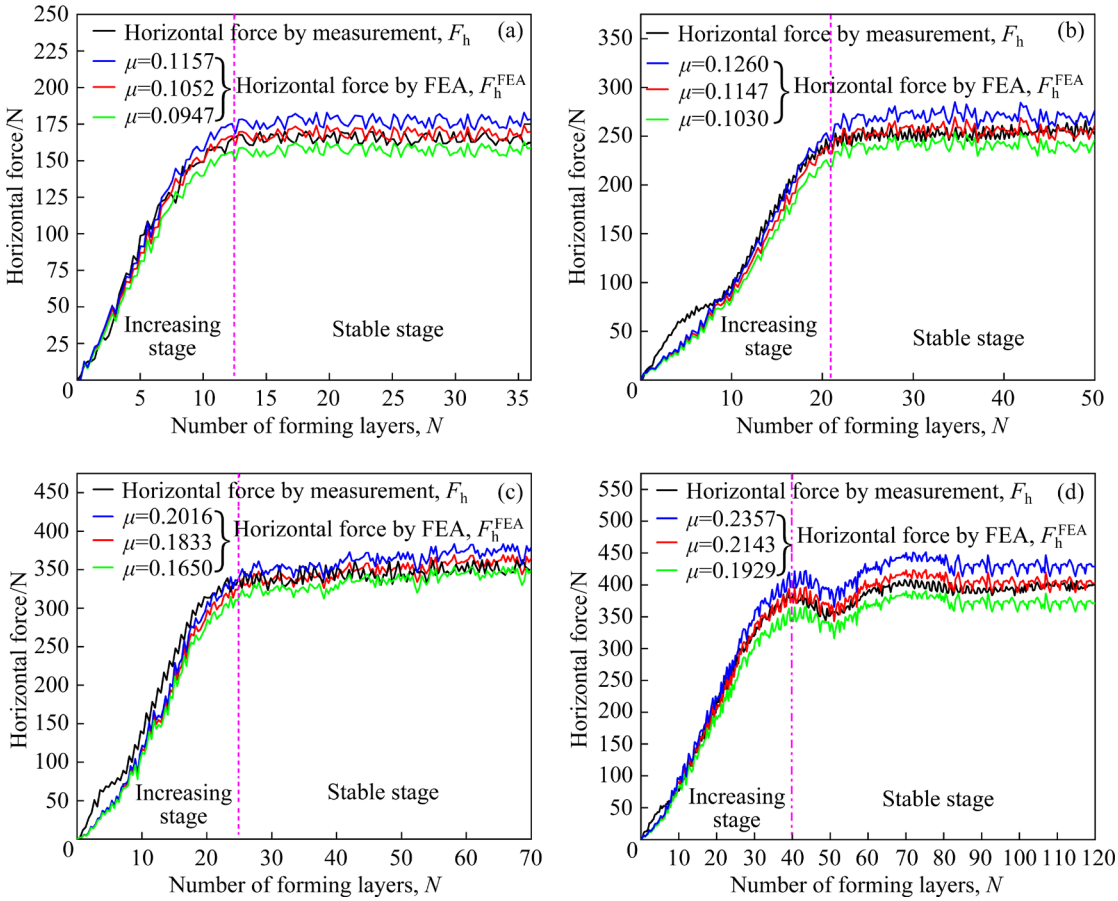

Fig. 13 Simulated and measured horizontal forces with different wall angles: (a) α=30°; (b) α=40°; (c) α=50°; (d) α=60°

behavior trend obtained in the present study.

$$\mu^* = F_h / F_z \tag{42}$$

The friction coefficient and fraction indicator increase with the increase in wall angle, regardless of the specific plane curve feature, as shown in Fig. 14(a). Furthermore, the friction indicators of different plane curves are basically identical at the same wall angle. The measured friction coefficients also have similar behavior. This trend remains consistent when forming along the spiral and contour process paths, as shown in Fig. 14(b). Additionally, the friction indicators for both paths align well when the wall angles are identical, and so do the friction coefficients. Although the values differ under various lubrication conditions (L-HM46 oil, MoS_2 grease, graphite powder, and dry friction), the changing trends remain constant, as shown in Figs. 14(c) and (d). That is, the friction coefficient is minimal with L-HM46 oil lubrication, slightly increases with MoS_2 grease lubrication, continues to grow with graphite powder lubrication, and is the most pronounced under dry friction condition without the lubrication. In addition, all increase with the increase of the wall angle.

According to the above analysis, the changing trends of friction coefficients and friction indicators with the wall angle are basically the same under different plane curves, process paths, and lubrication conditions.

The influence of plane curves on the friction test results is analyzed based on μ_{base}^{1111}, μ_{base}^{2111}, μ_{base}^{3111}, and μ_{base}^{4111}, as shown in Fig. 15(a). The change rate of friction coefficient (η) is calculated by using Eq. (43). The friction coefficients of the truncated pyramid and truncated elliptic cone change by 4.658% and 2.757% at α=30°, by 4.098% and 3.139% at α=40°, by 3.710% and 0.491% at α=50°, and by 2.774% and 2.945% at α=60°, respectively. The variation of friction coefficients is slight, and the maximum is only 4.658%. The friction conditions appear to be largely independent of the features associated with the plane curve. Therefore, the friction test results obtained from parts with a single plane curve feature can be employed to anticipate the friction conditions of parts with more intricate plane curve features.

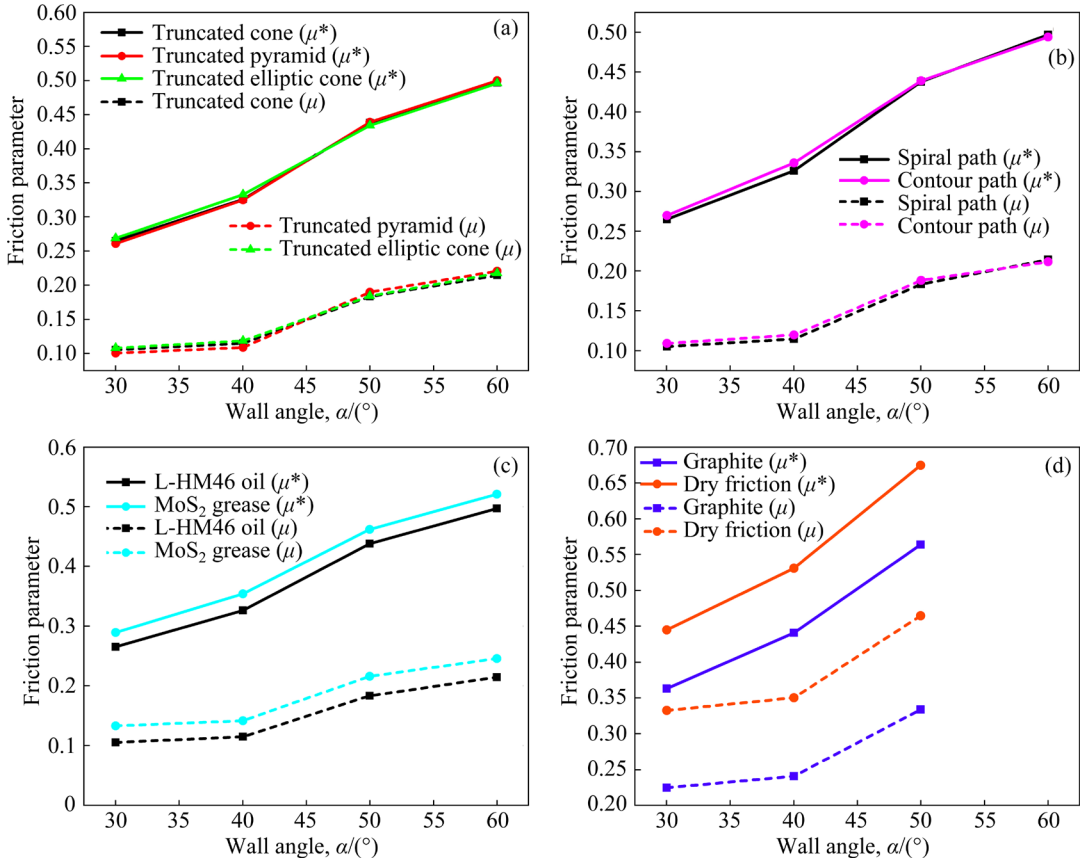

Fig. 14 Friction indicator and fraction coefficient under different friction conditions: (a) Different plane curves; (b) Different paths; (c) L-HM46 oil and MoS_2 grease; (d) Graphite powder and dry friction

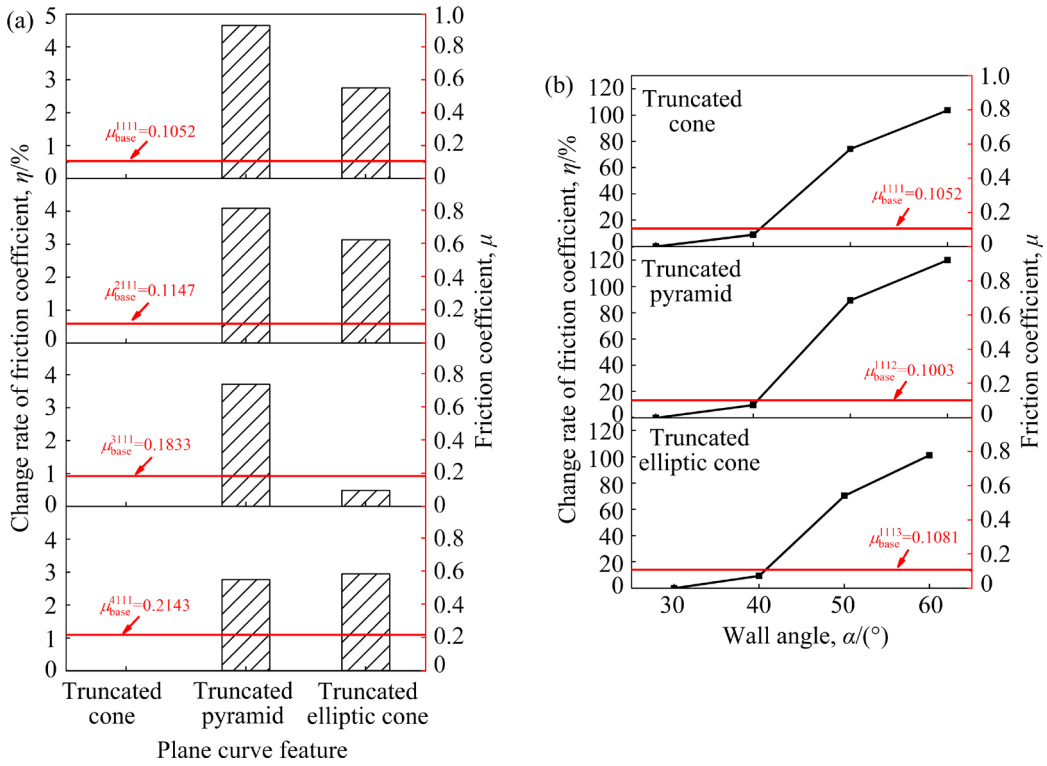

Fig. 15 Influence of plane curve features (a) and wall angles (b) on friction test results

$$\eta=\frac{\left|\mu_{\text{others}}^{ijkn}-\mu_{\text{base}}^{ijkn}\right|}{\mu_{\text{base}}^{ijkn}}\times 100\% \tag{43}$$

where μ_{base}^{ijkn} is the friction coefficient for the basic parameters; $\mu_{\text{others}}^{ijkn}$ represents the friction coefficient under other conditions compared to the forming conditions represented by the base coefficient. Here, i ranges from 1 to 4, corresponding to α values of 30°, 40°, 50°, and 60°, respectively; j ranges from 1 to 4, representing L-HM46 oil, MoS_2 grease, graphite, and dry friction conditions, respectively; k ranges from 1 to 2, corresponding to the special path and contour path in the forming process, respectively; n ranges from 1 to 3, representing the truncated cone, truncated pyramid, and truncated elliptic cone plane curves, respectively.

The influence of wall angle on the friction test results is discussed based on μ_{base}^{1111}, μ_{base}^{1112} and μ_{base}^{1113}, as shown in Fig. 15(b).

The friction coefficients of the truncated cone, truncated pyramid and truncated elliptic cone increase by 9.03%, 9.671% and 9.436% at α=40°, by 74.24%, 89.531% and 70.398% at α=50°, and by 103.707%, 120.14% and 101.11% at α=60°, respectively. Therefore, compared with α=30°, the change rates at α=40° are less than 10%. Considering that this change has no noticeable effect on ISF, a smaller wall angle can be inferred to have minimal effect on the friction test results. However, the change rate increases remarkably after $\alpha>40°$, which shows that a larger wall angle considerably affects the friction test results. Thus, the influence of wall angle is as follows: the friction coefficient remains essentially stable with smaller wall angles and gradually intensifies as the wall angle increases. Therefore, the friction coefficient can be assessed at any wall angle within the range for parts with $\alpha\leq 40°$. For parts with $\alpha>40°$, the friction coefficient can be evaluated on the basis of the actual wall angle.

For a more detailed evaluation of the differences in friction test results between the two process paths, the deviation in friction coefficients was calculated at wall angles of 30°, 40°, 50°, and 60°. The results are depicted in Fig. 16(a) based on the data presented in Fig. 10(b). The deviations between the spiral and contour paths at wall angles of 30°, 40°, 50°, and 60° are 3.707%, 4.446%, 2.619%, and 1.213%, respectively. Notably, a close agreement is observed between the friction test results of the two process paths, suggesting that the

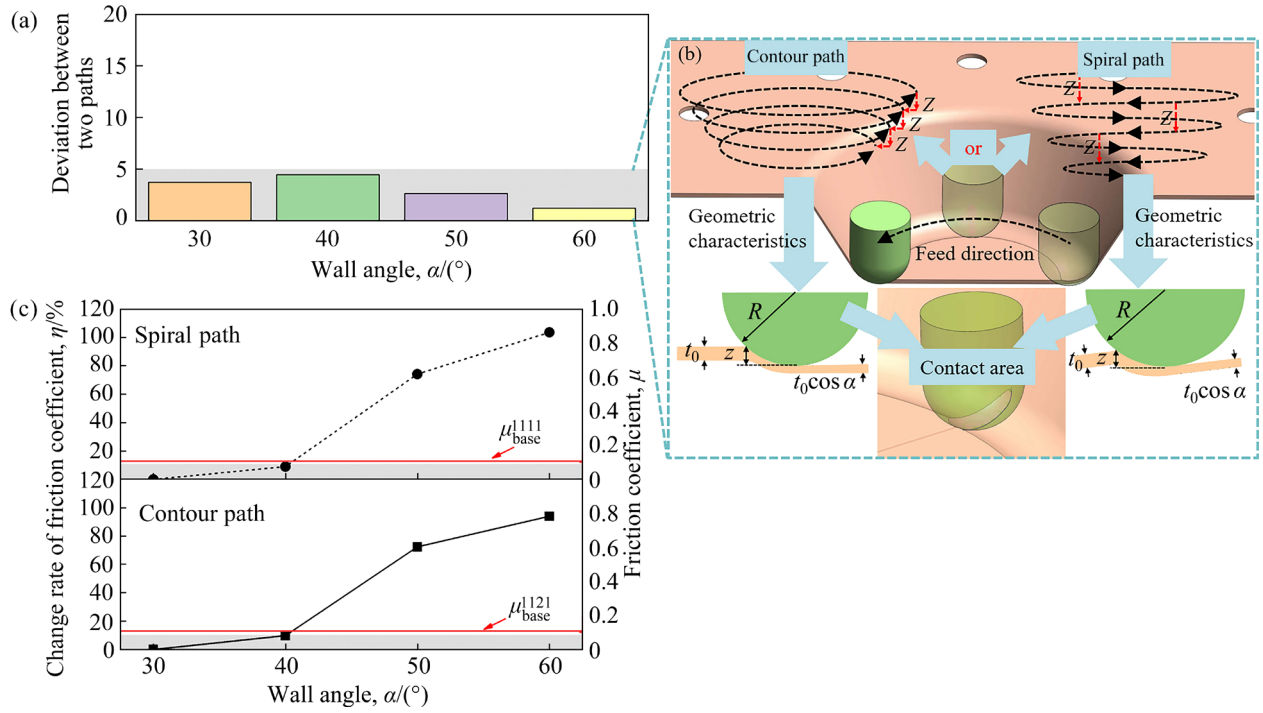

Fig. 16 Influence of process paths and wall angles on friction test results: (a) Deviation between contour and spiral paths at different wall angles; (b) Contact area during forming along contour and spiral paths; (c) Change rate of friction coefficient (η) with wall angles under different process paths

friction conditions in ISF are minimally affected by the chosen process path.

The contact area during forming along the contour and spiral paths is shown in Fig. 16(b). Regardless of the process path, when the depth increment of the adjacent forming layers is Z, other forming parameters are identical. According to Eqs. (8)−(11), the contact areas of the two process paths are equal. Therefore, with different process paths but identical other forming parameters, the friction test results are consistent due to the identical contact area, surface stress state, and lubrication conditions.

To evaluate quantitatively the influence of wall angles on friction coefficients across distinct process paths, the friction test results depicted in Fig. 10(b) were proceeded using Eq. (43). The results are illustrated in Fig. 16(c). For the spiral path, the friction coefficient at α=30° (0.1052) served as the baseline, denoted as μ_{base}^{1111}. The rates of change for α=40°, 50°, and 60° were found to be 9.030%, 74.240%, and 103.707%, respectively. Similarly, for the contour path, by utilizing the friction coefficient at α=30° (0.1091) as the baseline, designated as μ_{base}^{1121}, the rates of change for α=40°, 50°, and 60° were computed as 9.808%, 72.411%, and 94.042%, respectively. The results clearly indicate that the friction test results in both paths remain stable when $\alpha < 40°$. By contrast, the friction test results increase remarkably when $\alpha > 40°$. The influence of wall angle on friction test results exhibits a consistent trend irrespective of the process path.

Equation (43) is used to analyze results from Fig. 10(c) and quantitatively evaluate the influence of lubrication conditions and wall angle on friction coefficients. Change rates in friction coefficients at wall angles of 30°, 40°, 50°, and 60° under various lubrications are depicted in Fig. 17(a), using L-HM46 oil lubrication as a baseline (μ_{base}^{1111}, μ_{base}^{2111}, μ_{base}^{3111} and μ_{base}^{4111}). The results show a remarkable increase in friction coefficients under MoS_2 grease, graphite, and dry friction conditions. At α=30°, the increase relative to L-HM46 oil is 26.331% for MoS_2 grease, 113.688% for graphite, and 216.160% for dry friction. At α=40°, the increase relative to L-HM46 oil is 23.191% for MoS_2 grease, 110.026% for graphite, and 205.405% for dry friction. Similarly, at α=50°, the increase relative to L-HM46 oil is 17.676% for MoS_2 grease, 82.160% for graphite, and 153.519% for dry friction, and at α=60°, MoS_2 grease lubrication led to a 14.512%

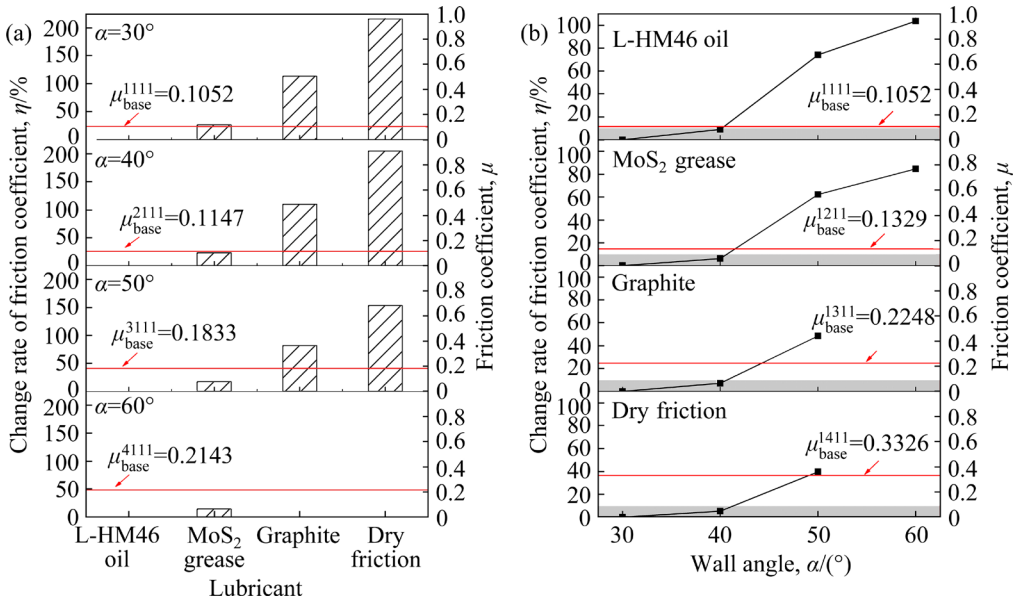

Fig. 17 Influence of lubricants and wall angles on friction test results: (a) Change rate of friction coefficient (η) with lubrication conditions at different wall angles; (b) Change rate of friction coefficient (η) with wall angles under different lubrication conditions

increase compared with L-HM46 oil lubrication. Overall, regardless of the wall angle, lubrication conditions considerably influenced the friction coefficient.

Friction coefficient is the lowest with L-HM46 oil lubrication, and compared with this condition, the change rates increased continuously for MoS_2 grease, graphite, and dry friction, especially the latter two. L-HM46 oil and MoS_2 grease played a lubricating role, resulting in a relatively reduced friction coefficient. Graphite powder is prone to be expelled from the interface, leading to poor lubrication effects, and under dry friction conditions, severe friction effects occurred, causing a remarkable increase in the friction coefficient. Given the influence of friction on material formability, parts with large wall angles cannot be formed under poor friction conditions. Moreover, poor friction conditions may induce a surface orange peel effect and considerably reduce part usability. Therefore, friction coefficient should be appropriately reduced to improve the formability and surface quality in actual forming.

In Fig. 17(b), friction coefficients at α=30° under L-HM46 oil, MoS_2 grease, graphite, and dry friction conditions are taken as baseline values (μ_{base}^{1111}, μ_{base}^{1211}, μ_{base}^{1311}, and μ_{base}^{1411}). The changes in friction coefficients at high wall angles are then calculated. With L-HM46 oil lubrication, friction coefficients increase by 9.03%, 74.24%, and 103.707% at wall angles of 40°, 50°, and 60°, respectively. For MoS_2 grease lubrication, the fraction coefficients rise by 6.321%, 62.302%, and 84.650% at these angles. With graphite lubrication, change rates are 7.162% and 48.532% at wall angle of 40° and 50°, respectively, while dry friction shows change rates of 5.322% and 39.717% at these angles. These results indicate a consistent trend where the friction coefficient change rate is less than 10% up to a wall angle of 40°, indicating insensitivity to small wall angle variations. Therefore, for parts with wall angles below 40°, friction coefficients can be considered stable in the production. However, at wall angles above 40°, the friction coefficient changes considerably, suggesting a sensitivity to wall angle variations and necessitating specific evaluations for parts with wall angles above 40° in manufacturing process.

6 Conclusions

(1) A semi-analytical friction test method was proposed for ISF. Firstly, the instantaneous contact area model was constructed by considering the loading history. Then, the analytical model of contact stress was established in line with the

Tresca yield criterion. The horizontal force analytical model was developed in combination with the analytical model of deformation force as determined by the above two analytical models with the direction of friction of ISF. The friction coefficient was calculated by using an equilibrium relationship established between the analytical model and the measured value.

(2) The accuracy of the model was assessed by comparing the predicted values of deformation force and forming force with the experimental values and the predicted values of other methods. The accuracy of the evaluated friction coefficient was verified through comparison between the measured horizontal forces and the FEA ones of different friction coefficients. The accuracy of the evaluated trend of changes in friction coefficient was confirmed by analyzing the trend of changes in friction coefficients and friction indicators under various forming conditions.

(3) Plane curve features minimally affect friction conditions. Therefore, the friction condition of a complex geometric part can be evaluated using that of a part with simple plane curve features. Friction is not sensitive to process path changes but is considerably affected by lubrication condition, with L-HM46 oil showing the least friction, followed by MoS_2 grease, graphite powder, and dry condition. Friction sensitivity to wall angle is minimal below 40°, but becomes remarkable above this angle, requiring specific evaluations based on the actual wall angle.

CRediT authorship contribution statement

Guang-can YANG: Conceptualization, Methodology, Investigation, Data curation, Formal analysis, Writing − Original draft, Writing − Reviewing and editing; **Da-wei ZHANG:** Conceptualization, Formal analysis, Writing − Reviewing and editing; **Chong TIAN:** Sample preparation, Writing − Reviewing and editing; **Sheng-dun ZHAO:** Supervision.

Declaration of competing interest

The authors declare that they have no known competing financial interests or personal relationships that could have appeared to influence the work reported in this paper.

Acknowledgments

The authors would like to gratefully acknowledge the financial support from the National Key R&D Program of China (No. 2023YFB3407003), and the National Natural Science Foundation of China (No. 52375378).

References

[1] LÓPEZ-FERNÁNDEZ J A, CENTENO G, MARTINEZ-DONAÍRE A J, MORALES-PALMA D, VALLELLANO C. Stretch-flanging of AA2024-T3 sheet by single-stage SPIF [J]. Thin-Walled Structures, 2021, 160: 107338.

[2] AL-GHAMD K A, HUSSAIN G. Bulging in incremental sheet forming of cold bonded multi-layered Cu clad sheet: Influence of forming conditions and bending [J]. Transactions of Nonferrous Metals Society of China, 2019, 29: 112−122.

[3] ROUX P. Machines for shaping sheet metal: United States Patent, US 2945528 [P]. 1960−07−19.

[4] AL-GHAMDI K A, HUSSAIN G. Threshold tool-radius condition maximizing the formability in SPIF considering a variety of materials: Experimental and FE investigations [J]. International Journal of Machine Tools and Manufacture, 2015, 88: 82−94.

[5] ULLAH S, LI Xiao-qiang, XU Peng, LI Yan-le, HAN Kai, LI Dong-sheng. A toolpath strategy for improving geometric accuracy in double-sided incremental sheet forming [J]. Chinese Journal of Aeronautics, 2023, 36(1): 468−479.

[6] JESWIET J, MICARI F, HIRT G, BRAMLEY A, DUFLOU J, ALLWOOD J. Asymmetric single point incremental forming of sheet metal [J]. CIRP Annals, 2005, 54: 88−114.

[7] ZHANG Qing-lai, XIAO Fu-gui, GUO Hai-ling, LI Chang-sheng, GAO Lin, GUO Xing-wu, HAN Wei-dong, BONDAREV A B. Warm negative incremental forming of magnesium alloy AZ31 sheet: New lubricating method [J]. Journal of Materials Processing Technology, 2010, 210(2): 323−329.

[8] SEN N, SIRIN S, KLVAK T, CIVEK T, SECGIN O. A new lubrication approach in the SPIF process: Evaluation of the applicability and tribological performance of MQL [J]. Tribology International, 2022, 171: 107546.

[9] YANG Guang-can, ZHANG Da-wei, TIAN Chong, ZHAO Sheng-dun. Influence of geometric configurations on friction characteristics during incremental forming process of AA5052 sheet metal [J]. Transactions of Nonferrous Metals Society of China, 2025, 35: 715−733.

[10] HAGAN E, JESWIET J. Analysis of surface roughness for parts formed by computer numerical controlled incremental forming [J]. Proceedings of the Institution of Mechanical Engineers (Part B): Journal of Engineering Manufacture, 2004, 218: 1307−1312.

[11] DURANTE M, FORMISANO A, LANGELLA A. Comparison between analytical and experimental roughness values of components created by incremental forming [J]. Journal of Materials Processing Technology, 2010, 210(14): 1934−1941.

[12] KISHORE J, JOSE F D, ANA R, SILVA M B. Microstructural investigation and lubrication study for single point incremental forming of copper [J]. International

Journal of Solids and Structures, 2018, 151: 145−151.

[13] HUSSAIN G, GAO L D, HAYAT N, CUI Z, PANG Y C, DAR N U. Tool and lubrication for negative incremental forming of a commercially pure titanium sheet [J]. Journal of Materials Processing Technology, 2008, 203(1/2/3): 193−201.

[14] KIM Y H, PARK J J. Effect of process parameters on formability in incremental forming of sheet metal [J]. Journal of Materials Processing Technology, 2002, 130: 42−46.

[15] AZEVEDO N G, FARIAS J S, BASTOS R P, TEIXEIRA P, DAVIM J P, SOUSA R J A D. Lubrication aspects during single point incremental forming for steel and aluminum materials [J]. International Journal of Precision Engineering and Manufacturing, 2015, 16: 589−595.

[16] ZHANG Shuo-wen, ZHANG Da-wei, ZHAO Sheng-dun, JIANG Fei, LEE M G. Characteristics of surface and subsurface of formed thread parts by axial-infeed thread rolling process [J]. Chinese Journal of Aeronautics, 2023, 36(3): 471−481.

[17] ZHANG Da-wei, YANG Guang-can, ZHAO Sheng-dun. Frictional behavior during cold ring compression process of aluminum alloy 5052 [J]. Chinese Journal of Aeronautics, 2021, 34(5): 47−64.

[18] HU Yong, ZHANG Xu, JIA Hui-bin, WANG Shao-hui, CHAI Li-qiang. Fretting wear behavior and wear mechanism of IN738LC alloy formed by selective laser melting [J]. The Chinese Journal of Nonferrous Metals, 2024, 34: 1−12. (in Chinese)

[19] BAMBACH M. A geometrical model of the kinematics of incremental sheet forming for the prediction of membrane strains and sheet thickness [J]. Journal of Materials Processing Technology, 2010, 210(12): 1562−1573.

[20] ALLWOOD J M, SHOULER D R, TEKKAYA A E. The increased forming limits of incremental sheet forming processes [J]. Key Engineering Materials, 2007, 344: 621−628.

[21] EYCKENS P, DUFLOU J, van BAEL A, van HOUTTE P. The significance of friction in the single point incremental forming process [J]. International Journal of Material Forming, 2010, 3: 947−950.

[22] CHANG Zhi-dong, CHEN Jun. Mechanism of the twisting in incremental sheet forming process [J]. Journal of Materials Processing Technology, 2020, 276: 116396.

[23] CARRINO L, DI MEO N, SORRENTINO L, STRANO M. The influence of friction in the negative dieless incremental forming process [C]//Proceedings of the 9th International ESAFORM Conference on Material Forming. Glasgow, PA: AKAPIT, 2006: 207−210.

[24] JACKSON K, ALLWOOD J. The mechanics of incremental sheet forming [J]. Journal of Materials Processing Technology, 2009, 209(3): 1158−1174.

[25] DUNCAN J L, SHABEL B S, FILHO J G. A tensile strip test for evaluating friction in sheet metal forming [C]//SAE Technical Paper Series. Detroit, Michigan, USA: SAE International, 1978: 780391.

[26] ANDREASEN J L, OLSSON D D, CHODNIKIEWICZ K, BAY N. Bending under tension test with direct friction measurement [J]. Proceedings of the Institution of Mechanical Engineers (Part B): Journal of Engineering Manufacture, 2006, 220(1): 73−80.

[27] ANDREASEN J L, BAY N, ANDERSEN M, CHRISTENSEN E, BJERRUM N. Screening the performance of lubricants for the ironing of stainless steel with a strip reduction test [J]. Wear, 1997, 207(1/2): 1−5.

[28] NINE H D. Mechanics of sheet metal forming [M]. Boston, MA: Springer, 1978: 179−211.

[29] BAY N, OLSSON D D, ANDREASEN J L. Lubricant test methods for sheet metal forming [J]. Tribology International, 2008, 41(9/10): 844−853.

[30] WANG W, WAGONER R H. A realistic friction test for sheet forming operations [C]//SAE Technical Paper Series. Detroit, Michigan, USA: SAE International, 1993, 930807.

[31] HAMILTON K A S. Friction and external surface roughness in single point incremental forming: A study of surface friction, contact area and the ‘orange peel’ effect [D]. Canada: Department of Mechanical and Materials Engineering, Queen’s University, 2010: 21−23.

[32] SILVA M B, SKJOEDT M, MARTINS P A F, BAY N. Revisiting the fundamentals of single point incremental forming by means of membrane analysis [J]. International Journal of Machine Tools and Manufacture, 2008, 48(1): 73−83.

[33] LU Bin, FANG Yong-yong, XU Dong-kai, CHEN Jun, OU H A, MOSER N H, CAO Jian. Mechanism investigation of friction-related effects in single point incremental forming using a developed oblique roller-ball tool [J]. International Journal of Machine Tools and Manufacture, 2014, 85: 14−29.

[34] LI Yan-le, LIU Zhao-bing, DANIEL W J T B, MEEHAN P A. Simulation and experimental observations of effect of different contact interfaces on the incremental sheet forming process [J]. Materials and Manufacturing Processes, 2014, 29(2): 121−128.

[35] DURANTE M, FORMISANO A, LANGELLA A, CAPECE MINUTOLO F M. The influence of tool rotation on an incremental forming process [J]. Journal of Materials Processing Technology, 2009, 209(9): 4621−4626.

[36] XU Dong-kai, WU Wei-chao, MALHOTRA R, CHEN Jun, LU Bin, CAO Jian. Mechanism investigation for the influence of tool rotation and laser surface texturing (LST) on formability in single point incremental forming [J]. International Journal of Machine Tools and Manufacture, 2013, 73: 37−46.

[37] ASGHAR J, LINGAM R, SHIBIN E, REDDY N. Tool path design for enhancement of accuracy in single-point incremental forming [J]. Proceedings of the Institution of Mechanical Engineers (Part B): Journal of Engineering Manufacture, 2014, 228(9): 1027−1035.

[38] BANSAL A, LINGAM R, YADAV S K, REDDY N V. Prediction of forming forces in single point incremental forming [J]. Journal of Manufacturing Processes, 2017, 28(pt.3): 486−493.

[39] CHANG Zhi-dong, LI Ming, CHEN Jun. Analytical modeling and experimental validation of the forming force in several typical incremental sheet forming processes [J]. International Journal of Machine Tools and Manufacture, 2019, 140: 62−76.

[40] LIU Fu-yuan, LI Xiao-qiang, LI Yan-le, WANG Zi-jian,

ZHAI Wei-dong, LI Fang-yi, LI Jian-feng. Modelling of the effects of process parameters on energy consumption for incremental sheet forming process [J]. Journal of Cleaner Production, 2020, 250: 119456.

[41] YANG Zhi-yun, CHEN Fei. Mechanism of twist in incremental sheet forming of thermoplastic polymer [J]. Materials & Design, 2020, 195: 108997.

[42] AERENS R, EYCKENS P, van BAEL A, DUFLOU J R. Force prediction for single point incremental forming deduced from experimental and FEM observations [J]. The International Journal of Advanced Manufacturing Technology, 2010, 46: 969−982.

板材渐进成形中一种新的摩擦测试方法

杨光灿，张大伟，田 冲，赵升吨

西安交通大学 机械工程学院，西安 710049

摘 要：构建了板材渐进成形中考虑加载历史的接触面积和接触应力分析模型，然后将其与该工艺摩擦力方向特征和水平力结合，提出了一种能反映板材渐进成形特性的摩擦测试方法。测量了在不同平面曲线、工艺路径和润滑条件下成形不同壁角零件时的摩擦因数。通过与试验、仿真以及与其他模型对比分析的方法验证了分析模型和测定的摩擦因数及其变化趋势的准确性。研究发现，零件平面曲线特征和工艺路径对摩擦因数的影响不显著；而在 L-HM46 油、MoS_2 润滑脂、石墨粉末润滑及干摩擦条件下，摩擦因数呈逐渐增大的变化趋势；值得注意的是，当壁角≤40°时，摩擦因数保持相对恒定，但当壁角超过 40°后，摩擦因数逐渐增大。

关键词：板材渐进成形；摩擦测试方法；接触面积；摩擦因数；成形力

(Edited by Wei-ping CHEN)